Mineralogy and Petrology (2022) 116:137–149
https://doi.org/10.1007/s00710-022-00773-3

ORIGINAL PAPER

Orthopyroxene rim growth during reaction of (Co, Ni, Mn, Zn)-doped forsterite and quartz: Experimental constraints on element distribution and grain boundary diffusion

Sarah Incel[1] · **Ralf Milke**[2] · **Bernd Wunder**[3]

Received: 27 July 2021 / Accepted: 27 January 2022 / Published online: 25 February 2022

Abstract
Mantle metasomatism is an important process in subduction zones in which fluids from the dehydrating oceanic slab interact with the overlying upper mantle resulting in a chemical alteration of the mantle. Consequently, this fluid-rock interaction may influence the mantle rock's physical properties such as the deformation behavior. In order to study element redistribution during mantle metasomatism in the laboratory, we used the simplified model reaction olivine + quartz = orthopyroxene, where olivine acts as representative for the upper mantle and quartz as proxy for the metasomatizing agent. We conducted piston-cylinder experiments at 1.5 GPa and 950 to 1400 °C, lasting between 48 and 288 h, on samples containing a mixture of quartz and one set of synthesized forsterite samples doped with either Co, Ni, Mn, or Zn. Additionally, we tested the influence of either nominally anhydrous or hydrous experimental conditions on the chemical distribution of the respective dopant element by using either crushable alumina or natural CaF_2 as pressure medium. Results of the chemical analyses of the recovered samples show dopant specific partitioning between doped forsterite and orthopyroxene independent of the confining pressure medium; except for the runs in which Ni-doped forsterite samples were used. The observed Ni- and Co-enrichment in forsterite samples may be used to identify mantle rocks that underwent mantle metasomatism in nature.

Keywords Mantle metasomatism · Orthopyroxene rim growth · Doped forsterite samples · Piston-cylinder experiments

Introduction

The formation of pyroxenite veins in peridotites can be explained by the interaction between peridotites and an external silicon enriched fluid or melt, e.g., in subduction zones where dehydration-derived fluids from the descending slab interact with the overlying olivine-rich mantle wedge (Bodinier et al. 1989; Borghini et al. 2020, 2016, 2013; Cvetković et al. 2007; Hidas et al. 2021; Wulff-Pedersen et al. 1999). The interaction between peridotites and fluids or melts is called mantle metasomatism. In order to better understand natural processes, such as mantle metasomatism, mostly occurring in chemically complex systems, model reactions are needed that are on the one hand simple enough to assess the underlying chemical and physical mechanisms and on the other hand still comparable to natural systems. The model reaction of choice to investigate mantle metasomatism is orthopyroxene (Opx) rim growth between olivine (Ol), as a proxy for Earth's mantle, and quartz (Qz), representative for the Si-rich metasomatizing agent (e.g., Abart et al. 2004; Fisler et al. 1997; Gardés et al. 2011; Milke et al. 2001; Yund 1997 and references therein). Since Ol and Qz are not in chemical equilibrium, they will react to produce an orthopyroxene rim separating both reactants. The Opx forming reaction between Ol and Qz is Ol + Qz → 2 Opx.

At sufficiently high temperatures that allow the diffusive redistribution of chemical components, an Opx rim phase with a thickness of a few micrometers forms within common laboratory time scales of several hours to days. Previous

Editorial handling: S. W. Faryad

✉ Sarah Incel
sarah.incel@rub.de

[1] Institute for Geology, Mineralogy, and Geophysics, Ruhr-Universität Bochum, Universitätsstr. 150, Bochum 44780, Germany

[2] Institute of Geological Sciences, Freie Universität Berlin, Malteserstr. 74-100, Berlin 12249, Germany

[3] Helmholtz-Zentrum Potsdam, Deutsches GeoForschungsZentrum GFZ, Telegrafenberg, Potsdam 14473, Germany

studies experimentally demonstrated that enstatite grows between forsterite (Fo) and Qtz in equal amounts into both directions from the initial Fo-Qz interface indicating that rim growth is mostly controlled by MgO diffusion through the Opx layer (Abart et al. 2004; Milke et al. 2007, 2001). Of course, processes such as element diffusion may be significantly faster in a fluid-rock system than in this simplified solid–solid reaction.

Using natural olivines with $Fo_{90.1}$, a previous experimental study demonstrates a particular chemical zoning pattern of Fe that evolved during Opx rim growth (Milke et al. 2011). Considering equilibrium partitioning at the Ol|Opx interface, $En_{91.4}$ will replace a $Fo_{90.1}$ (Seckendorff and Neill 1993). To ensure overall mass balance, the excess X_{Fe} will be incorporated into Opx that replaces Qz resulting in $En_{88.0}$ next to the Opx|Qz interface. Thus, after some time, Fe liberated at the Ol|Opx interface diffuses from the Fe-poorer region next to Ol towards a Fe-enriched area next to Qz. This apparent paradox can be solved by considering the polycrystalline structure of the Opx rim. In the studied temperature range, grain boundary diffusion coefficients are about 3–5 orders of magnitude larger than those for volume diffusion (Joesten 1991). Therefore, obeying equilibrium partitioning at the Ol-replacement front and overall mass balance, Fe/Mg counter-diffusion through the rim phase takes place along grain boundaries that act as fast diffusion pathways. Because of quartz' limitation for cation exchange, Fe is not buffered at the Opx|Qz interface and any excess Fe will be incorporated into Opx replacing Qz (Milke et al. 2011). Since natural olivines can contain various other metal cations such as Ni in minor or trace amounts, Milke et al. (2011) observed a second chemical zoning pattern of Ni that is different to the Fe-zoning pattern. The authors demonstrated an enrichment front of Ni in the relict olivine grains ahead of the Ol-replacement front, but no zoning pattern within the Opx rim was detectable, because the Ni-concentration was below the microprobe's detection limit. Using a 1-dimensional diffusion model to predict the chemical distribution of Ni during Opx rim growth, the authors state that Ni-enrichment in Ol ahead of the Ol-replacement front would only be possible assuming that Ni-back diffusion into Ol is faster than the ratio of Ni volume diffusion in Ol and Ni diffusion in Opx grain boundaries. As a result, the Opx replacing a Ni-enriched Ol would successively incorporate more Ni in order to obey equilibrium partitioning at this interface. From these results the authors conclude that equilibrium partitioning of Fe, Mg, and Ni only plays a role in a narrow zone right at the Ol|Opx interface, but that the chemical distribution of these elements throughout most of the rim phase will be rather controlled by kinetic fractionation.

Chemical data of olivines of cratonic areas show Ni-concentrations in olivine of up to 3500 ppm, which is almost ten times higher than regular Ni concentrations in San Carlos olivines (Kelemen et al. 1998). The authors explain these elevated Ni-concentrations to be the result of metasomatism in the upper mantle. Strikingly the experimental results of Milke et al. (2011) on Opx-rim growth between natural San Carlos olivine and Qtz show the enrichment of Ni in the remnant olivine grains, which is well in accordance with the findings and the interpretation of Kelemen et al. (1998) based on chemical data from natural olivines.

The present study aims in experimentally investigating the distribution behavior of other metal cations such as Co, Mn, and Zn during Opx rim growth as well as to test the proposed Ni-distribution pattern of Milke et al. (2011) by using synthetic forsterite doped with either Co, Ni, Mn, or Zn. Although less relevant for mantle metasomatism due to slab dehydration, but important for processes such as grain boundary diffusion, we also studied if differences in water fugacity influence the cation's distribution behavior and if

Table 1 Details on the EPMA chemical analyses

Element	X-ray line	Crystal	Counting time [s]	Calibrant
Si	Kα	PETJ*; PETH	10*; 20	Olivine
Mg	Kα	TAP	10*; 20	Olivine
Co	Kα*; Lα	LIFH*; LDEI	10*; 20	Co (metal)
Ni	Kα*; Lα	LIF*; LDEI	10*; 20	Ni (metal)
Mn	Kα*; Lα	LDEI	10*; 20	Rhodonite
Zn	Kα*; Lα	TAP	10*; 20	Zn (metal)

*Settings for analyses using the Jeol JXA 8200 Superprobe system

All analyses were done with defocused electron beam

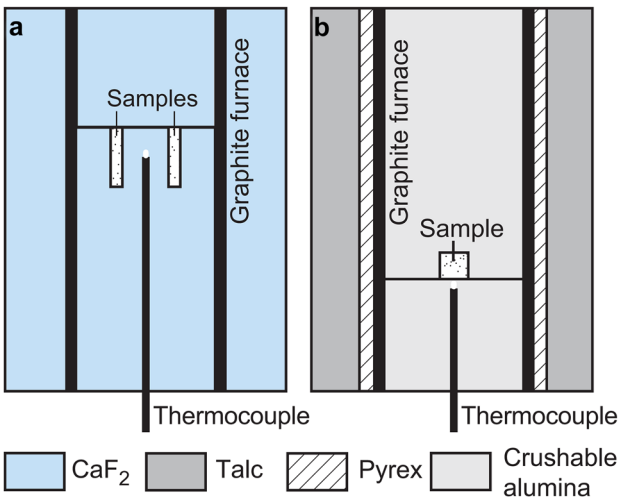

Fig. 1 Schematic drawing of the two sample assemblies used for the present experimental study. **a** Sample assembly for the hydrous runs. The pressure medium used is natural CaF_2. As shown, two samples find place in this sample assembly. **b** To create nominally anhydrous experimental conditions, we used crushable alumina as inner pressure medium that acts hygroscopically. The outer sleeve consisted of talc. Only one sample can be placed inside the assembly per run

Table 2 Experimental conditions and results of rim width measurements

Sample	Medium	T [°C]	Duration [h]	Rim width X [μm]	Squared rim width X^2 [μm^2]	N
Co–h-12.5	CaF_2	950	12.5	11.9 ± 1.0	165.2 ± 25.8	100
Co–h-48	CaF_2	950	48	14.4 ± 0.7	236.4 ± 23.0	250
Co–h-168	CaF_2	950	168	34.4 ± 1.0	1249.8 ± 76.2	245
Co-a-257	Crushable alumina	1200	257	27.2 ± 2.6	739.9 ± 176.9	100
Ni–h-12.5	CaF_2	950	12.5	12.4 ± 0.9	172.6 ± 26.2	88
Ni–h-48	CaF_2	950	48	10.3 ± 0.7	123.2 ± 15.3	154
Ni–h-168	CaF_2	950	168	15.0 ± 0.9	258.6 ± 32.3	147
Ni-a-120	Crushable alumina	1400	120	28.3 ± 0.6	814.8 ± 34.2	147
Zn-h-48	CaF_2	950	48	11.0 ± 1.4	126.4 ± 9.2	138
Zn-a-288	Crushable alumina	1100	288	19.7 ± 1.3	446.7 ± 67.0	127
Mn-h-48	CaF_2	950	48	9.2 ± 0.6	94.2 ± 11.3	96
Mn-a-18	Crushable alumina	1100	18	15.8 ± 0.5	254.5 ± 15.4	76

N number of measurements

Uncertainties are quoted at the 1σ level

the presence of a dopant element in forsterite has an impact on Opx rim growth rates.

Synthesis and analyses

Synthesis of doped forsterite and sample characterization

Doped forsterite samples (d-Fo) were synthesized by using a flux crystal growth method (Bloise et al. 2009). Four different sets of doped forsterite, Co-, Ni-, Mn-, and Zn-doped forsterite samples, were produced for the experiments. Hand-selected d-Fo crystals were chemically homogenized prior to the experiments by putting each set in a Pt cup closed with a Pt lid and placed in a furnace at around 1200 °C and ambient pressure for three days. Because volume diffusion coefficients for the selected dopant elements range between $10^{-14.57}$ m^2/s to $10^{-15.70}$ m^2/s in a temperature range of 1200 to 1300 °C (Petry et al. 2004; Spandler and O'Neill 2010) existing chemical gradients in the 100 to 500 μm large crystals will be either erased or reduced. The oxidizing conditions during this homogenization process were not controlled. Chemical analyses of the starting material and of the recovered samples after the piston-cylinder experiments were performed using two different electron probe micro-analyzer (EPMA) – a Jeol JXA 8200 Superprobe and a JEOL Hyperprobe JXA-8500F microprobe. The acceleration voltages for the chemical analyses were set to 15 and 8 kV, respectively. Further details on the EPMA chemical analyses are given in Table 1. For the line measurements we used a step size of 1 μm for analyses using the Jeol JXA 8200 Superprobe and a step size of 0.5 μm for analyses conducted using the JEOL Hyperprobe JXA-8500F microprobe.

Experimental methods

The samples used for the piston-cylinder experiments consisted of crystals from one set of doped forsterite samples, respectively, embedded in a quartz matrix in a weight ratio of 1:20. The grain size of the synthesized forsterite crystals selected for the experiments ranged from 100 to 500 μm and the quartz grains had a uniform size of approx. 50 μm. It has been shown that Fe–Mg diffusion in olivine varies as a function of crystal orientation (Chakraborty 1997), yet, investigation of the anisotropy of diffusion for each dopant element in forsterite was beyond the scope of the present study. Further, this study aims to qualitatively show potential differences in chemical distribution features of the dopant elements, which are not affected by anisotropy. For the sake of simplicity, we therefore assumed isotropic lattice diffusion. To qualitatively test the influence of water on the distribution behavior of the dopant elements during

Table 3 Chemical data of the doped forsterite samples prior to annealing

Dopant	SiO_2 [wt%]	MnO [wt%]	MgO [wt%]	ZnO [wt%]	CoO [wt%]	NiO [wt%]	Total [wt%]	N
Co	38.6 ± 0.3	-	41.2 ± 0.5	-	20.6 ± 0.4	-	100.4 ± 0.2	57
Ni	39.5 ± 0.1	-	50.7 ± 0.1	-	-	10.5 ± 0.03	100.7 ± 0.1	151
Mn	42.4 ± 0.4	1.2 ± 0.02	55.3 ± 0.5	-	-	0.1 ± 0.01	99.1 ± 0.1	135
Zn	41.6 ± 0.2	-	55.0 ± 0.2	1.5 ± 0.03	-	-	98.2 ± 0.1	81

N number of measurements

Uncertainties are quoted at the 2σ level

Opx rim growth, we used two different pressure media. It has been experimentally demonstrated that samples showing higher water concentrations relative to the surrounding pressure medium loose water due to hydrogen diffusion from the sample towards the pressure medium (Truckenbrodt and Johannes 1999). In an analogous manner, the water content in the sample increases in case there is a chemical gradient in water concentration from the pressure medium towards the sample. Therefore, in order to create hydrous experimental conditions during the piston-cylinder experiments, natural CaF_2 was used as pressure medium (Fig. 1). Natural CaF_2 always contains some amount of water, which will diffuse from the hydrous pressure medium into the sample during the experiment. Effectively dry conditions were established by using crushable alumina, which acts hygroscopically, as inner pressure medium (Fig. 1; Gardés et al. 2011). For the runs in which we used CaF_2 as pressure medium, the sample material was filled in platinum capsules and welded. The final sample size was approx. 1 cm in length and a few mm in width. For the runs in which we used crushable alumina we mechanically sealed the capsules, which had an outer diameter of 3 mm, an inner diameter of approx. 2.5 mm, and a height of 2 mm. Regardless of the pressure medium used, neither the powders nor the prepared samples were dried prior to the experiment. For the runs in which we used hydrous CaF_2 as pressure medium the sample name contains an 'h' and for the tests performed using crushable alumina the sample names contain an 'a'. Although we did not measure the water concentration initially present in the samples and were not able to monitor the evolution of the water concentration in the sample with time, we will call the samples that were surrounded with the hydrous CaF_2 as "hydrous" samples and those surrounded by crushable alumina as "anhydrous" samples.

Every experiment was performed under constant pressure and temperature conditions. First, the sample was pressurized to 1.5 GPa. After leaving it under pressure for around 1 h, heating started to either 950 °C, for the hydrous runs, or to varying temperatures (1100 to 1400 °C) for the nominally anhydrous runs (Table 2). The runs conducted under hydrous experimental conditions lasted 48 h, whereas the anhydrous runs were stopped after different durations due to unstable experimental conditions at elevated temperatures (Table 2). Based on the laboratory calibration using the quartz–coesite transition, a pressure correction of -15% was applied to account for frictional loss and the pressure accuracy is estimated to be ± 0.05 GPa (Gardés et al. 2011). The temperature was measured using a S-type thermocouple and the associated temperature error is assumed to be ± 20 °C (Gardés et al. 2011). In addition to the hydrous runs on Co- and Ni-doped forsterite samples that lasted 48 h, we conducted two experiments that were stopped after 12.5 and 168 h, respectively, in order to highlight the influence of the presence of Co and Ni on Opx-rim growth rates. After quenching and decompression, the recovered samples were embedded in epoxy, cut, polished, and carbon coated for the microstructural and chemical analyses. The Opx-rim widths were measured using ImageJ (Abràmoff et al. 2004). The number of measurements for each sample and the arithmetic mean of the measured rim widths are listed in Table 2. To investigate the chemical variations across the rims and within the relict doped forsterite, we conducted line measurements with a step size of either 0.5 µm or 1 µm and/or element distribution maps.

Table 4 Chemical formulae of the doped forsterite samples

Main dopant element	Chemical formula
Co	$Mg_{1.55}Co_{0.45}SiO_4$
Ni	$Mg_{1.75}Ni_{0.25}SiO_4$
Zn	$Mg_{1.97}Zn_{0.03}SiO_4$
Mn	$Mg_{1.97}Mn_{0.03}SiO_4$

Fig. 2 BSE images of the samples that experienced hydrous experimental conditions, i.e., pressure medium was CaF_2, after 48 h **a**, **c**, **e**, **g** and samples that experienced nominally anhydrous conditions by using hygroscopic crushable alumina as confining medium **b**, **d**, **f**, **h**. Both interfaces, but especially the d-Fo|Opx interfaces, are much smoother in samples surrounded by CaF_2 than in samples in which we used crushable alumina

Experimental results

Starting material

Results of chemical analyses of the d-Fo crystals prior to annealing are given in Table 3 and their corresponding mineral formulae are listed in Table 4. The highest dopant concentration was obtained for Co-doped olivine with ~ 20 wt% CoO. Ni-doped olivine contained ~ 10 wt% NiO, and Zn- and Mn-doped olivine contained only ~ 1.5 and ~ 1.2 wt% ZnO and MnO, respectively. Although natural olivines do not show such high concentrations of either dopant cation, we decided to synthesize doped forsterite samples showing high dopant concentration (> 400 ppm) allowing for the detection of any chemical gradients within the Opx rim and the relict doped forsterite crystals.

Chemical zoning

The microstructures of the recovered samples reveal rims that formed between doped forsterite and quartz matrix (Fig. 2). The rim phase has been identified as Opx using EPMA chemical analysis. In back-scattered electrons (BSE) mode, the Opx rims show varying brightness contrasts implying variations in chemical composition (Fig. 2).

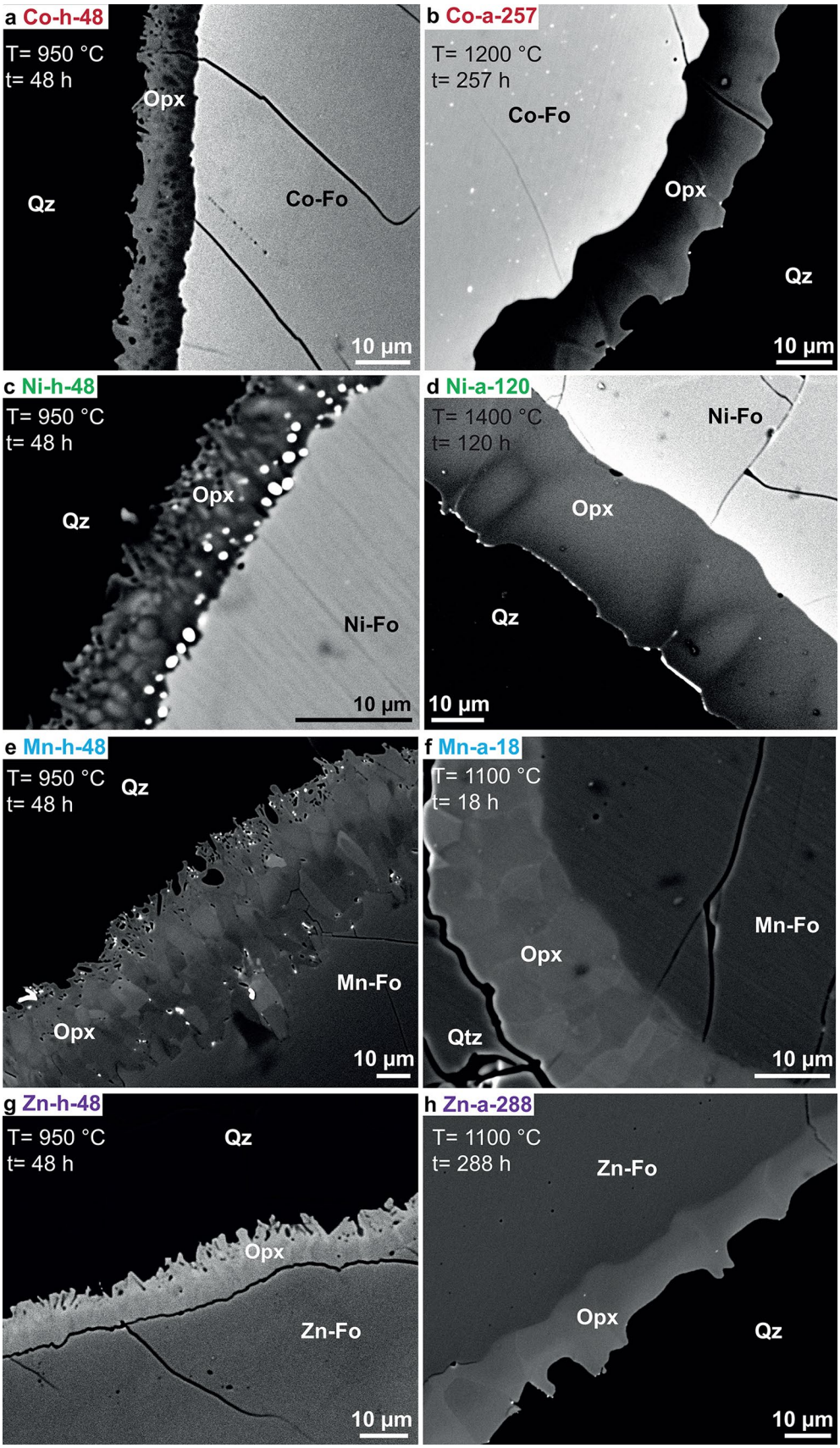
a Co-h-48
T= 950 °C
t= 48 h
Opx
Qz
Co-Fo
10 µm
b Co-a-257
T= 1200 °C
t= 257 h
Co-Fo
Opx
Qz
10 µm
c Ni-h-48
T= 950 °C
t= 48 h
Opx
Qz
Ni-Fo
10 µm
d Ni-a-120
T= 1400 °C
t= 120 h
Ni-Fo
Opx
Qz
10 µm
e Mn-h-48
T= 950 °C
t= 48 h
Qz
Mn-Fo
Opx
10 µm
f Mn-a-18
T= 1100 °C
t= 18 h
Mn-Fo
Opx
Qtz
10 µm
g Zn-h-48
T= 950 °C
t= 48 h
Qz
Opx
Zn-Fo
10 µm
h Zn-a-288
T= 1100 °C
t= 288 h
Zn-Fo
Opx
Qz
10 µm

Line measurements across the Opx rim, which developed around Co-doped forsterite, reveal that the darker inner part of the Opx rim adjacent to Co-Fo is depleted in Co relative to the brighter outer part next to Qz (red data points in Fig. 3a). Consequently, to ensure Opx stoichiometry, the Mg-concentration shows the exact opposite trend (black data points in Fig. 3a). The same Co- and Mg-concentration patterns are demonstrated in Co- and Mg-distribution maps of the nominally anhydrous sample Co-a-257 (Fig. 3b). Further, both data, the line measurement (0.5 µm step size) and the element distribution maps exhibit Co-enrichment in Co-Fo ahead of the Co-Fo-replacement front (Fig. 3). Another observation is the "bumpy" character of the Co-concentration across the Opx rim highlighted by the line measurement. Peaks in Co-concentration appear to correlate with the brighter Opx-grain rims including the Opx-grain boundaries and the valleys with the darker grain interiors (Fig. 3).

The presence of numerous spheres, appearing bright in BSE mode, in samples Ni–h-12.5, Ni–h-48, and Ni–h-168 hampers the investigation of existing chemical zoning patterns (Figs. 4a). Because most of the spheres are < 2 µm unambiguous quantitative chemical analyses were not possible. Element distribution maps of Ni–h-48 exhibit that these spheres are rich in Ni and contain S (Fig. 4b). Element distribution maps reveal that S contamination affected every set of doped forsterite samples and it is likely that S contamination is the result of the annealing in Pt-cups prior to the experiments. Microstructural analyses of the Ni-doped forsterite samples that lasted 12.5 h shows no precipitates within the rim but some at the Opx|Qz interface (Fig. 4a). The Opx rims in the sample on Ni-doped forsterite that was quenched after 168 h reveals rim parts exhibiting very few spheres mostly located at the Ni-Fo|Opx interface whereas other parts are highly decorated (Fig. 4a). Strikingly, the rim widths of these different regions are not significantly different. The BSE image showing the sample Ni–h-48 reveals no apparent gradient in Ni- and Mg-concentration of the bulk rim but rather on the grain size scale (Fig. 4a). Ni–h-48 exhibits Opx grains with brighter grain interiors relative to their surroundings, contrary to Co–h-48 (Figs. 4a and 3a). In sample Ni-a-120, which experienced nominally anhydrous experimental conditions, Ni-rich spheres are absent (Figs. 2d and 5a). A Ni-distribution map and a line measurement across the remnant Ni-Fo and the adjacent Opx rim with a step size of 1 µm demonstrate a Ni-enrichment front in Ni-Fo similar to the results of Milke et al. (2011) and a gradient in Ni concentration across the Opx rim with a decrease in Ni from the Ni-Fo|Opx interface towards the opposite Opx|Qz interface (Fig. 5). As for Ni–h-48, the Ni-map presented in Fig. 5a demonstrates Ni-richer Opx interiors relative to Ni-poorer Opx rims.

A line measurement with a step size of 0.5 µm exhibits that the Opx rims that formed around Mn-doped forsterite

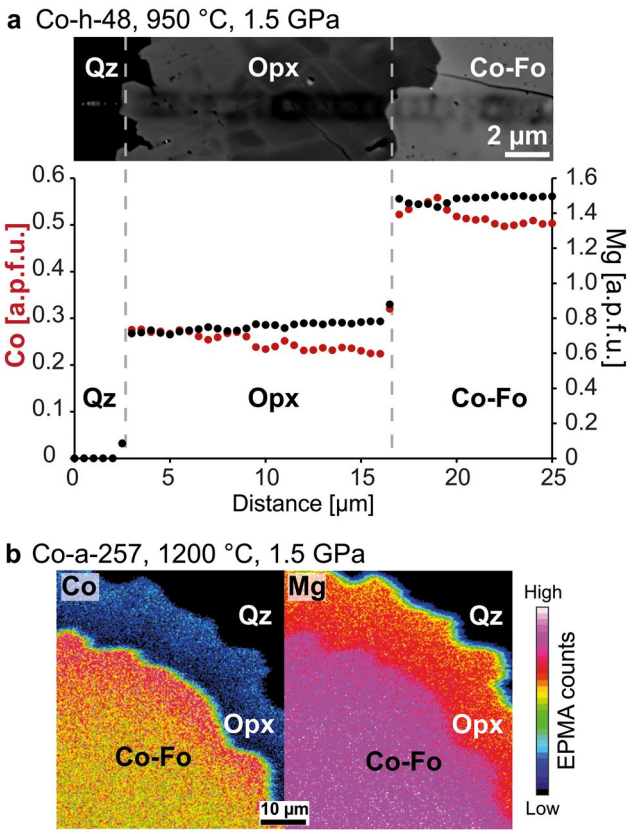

Fig. 3 Chemical data of Co–h-48 and Co-a-257. **a** Line scan across the Co-Fol|Opx interface and the Opx rim with a step size of 0.5 µm. Sizes of symbols exceed errors. **b** Co-distribution map (left) and Mg-distribution maps (right) of sample Co-a-257

under hydrous conditions does not reveal a striking gradient in Mn-concentration (Fig. 6a). The outer part of the Opx rim next to the Opx|Qz interface appears to be slightly enriched in Mn. The same pattern is shown in the Mn-distribution map of the nominally anhydrous counterpart Mn-a-18 (Fig. 6c). A line measurement with a step size of 0.5 µm across the Opx rim that formed around Zn-doped forsterite in Zn-h-48 shows a clear enrichment in Zn in the Opx part next to the Opx|Qz interface (Fig. 6b, d). The same is true for Zn-a-288 that experienced nominally anhydrous experimental conditions. From the line measurement and BSE images of the Opx rims around Zn-doped forsterite, it appears that Opx-grain rims are enriched in Zn relative to Opx interiors (Figs. 2g, h and 6b). Both dopant elements, Mn and Zn, show the same distribution behavior with a Mn or Zn enriched Opx rim next to the in the rim Opx|Qz relative to the Opx part adjacent to the Fo-Mn or Fo-Zn replacement front.

Rim and interface structure

The rim widths *X* of all samples are listed in Table 2. After 48 h under 950 °C and 1.5 GPa, the rims that developed

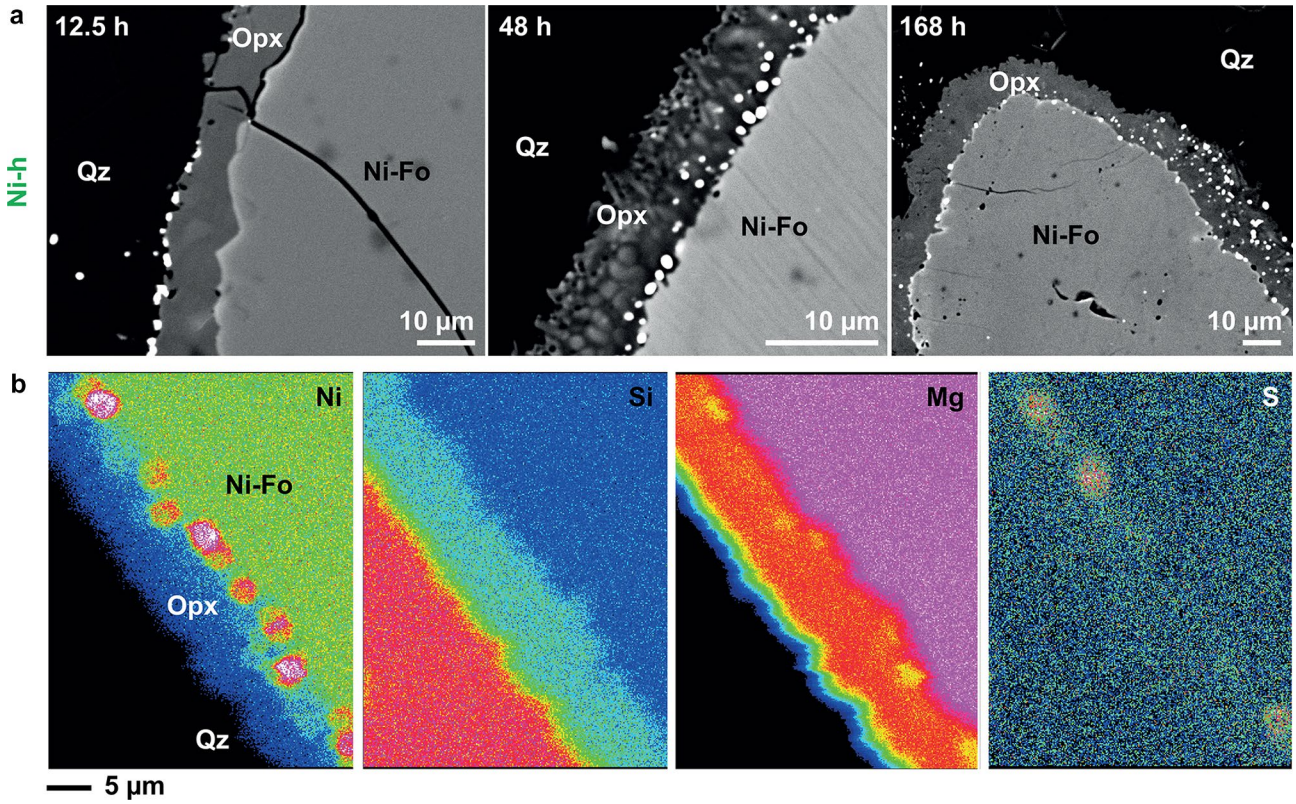

Fig. 4 **a** BSE images of the three runs on Ni-doped forsterite under hydrous conditions stopped after either 12.5, 48, or 168 h. Strikingly, after 168 h some parts of the rim show very few Ni-S-rich spheres whereas other regions exhibit plenty. **b** Element distribution maps (same general colour coding as in Fig. 3) of an Opx rim and the adjacent Ni-Fo and Qz matrix of the sample Ni–h-48

around Co-doped forsterite are with (14.4 ± 0.7) µm the widest and the Opx rims that formed around Mn-doped forsterite are with (9.2 ± 0.6) µm the thinnest. Because temperature and time were different for each sample, a direct comparison between the rim widths of the nominally anhydrous runs is hindered (Table 2). It is challenging to determine the Opx grain diameters using the BSE images, because in this setting and at this magnification we cannot unequivocally distinguish between grain rims and grain boundaries. Further, individual grains are difficult to recognize in Opx rims of the nominally anhydrous samples (Fig. 2). Therefore, we refrain from providing quantitative data on grain size, but compare the differences in appearance and the ratio between grain size to rim width between the hydrous and nominally anhydrous samples. Using the differences in brightness contrast in BSE mode to estimate Opx grain diameters, it seems that for the hydrous samples the ratio between Opx grain size to overall rim thickness is much smaller relative to the ratio between average Opx grain size and rim width of their anhydrous counterparts (Fig. 2). In Opx rims that formed around Co-, Ni-, and Zn-doped forsterite under nominally anhydrous conditions, individual Opx grains are often as large as the rim itself (Fig. 2b, d, f, h). Rims that grew in the Mn-a-18 sample show slightly smaller Opx grains relative to the other rims growing under nominally anhydrous conditions (Fig. 2b, d, f, h).

Both interfaces, the d-Fo|Opx and the Opx|Qz interface, appear much smoother in samples that experienced nominally anhydrous experimental conditions relative to their hydrous counterparts (Fig. 2). In the hydrous samples, the Opx|Qz interfaces are more uneven than the opposite d-Fo|Opx interface (Fig. 2a, c, e, g).

Rim growth rates

The rate constant k is the slope of the best-fit line through the data points in a squared rim width (X^2) vs. time (t) plot (Fig. 7). Within the error limits, there is no difference in rate constant k and thus in Opx rim growth rate between the experiments on natural olivines from Yund (1997) conducted at 1.4 GPa and 1000 °C and our data on Co-doped forsterite samples (Fig. 7). After shorter run durations of 12.5 h, the squared rim width obtained from our experiment on Ni-doped forsterite does not deviate significantly from the data on Co-doped forsterite and that from Yund (1997) conducted at 1.4 GPa and 1000 °C, but deviates significantly after 48 and 168 h. With a rim growth rate of around (1.6 ± 0.2) µm^2/h, Opx rims grow much slower

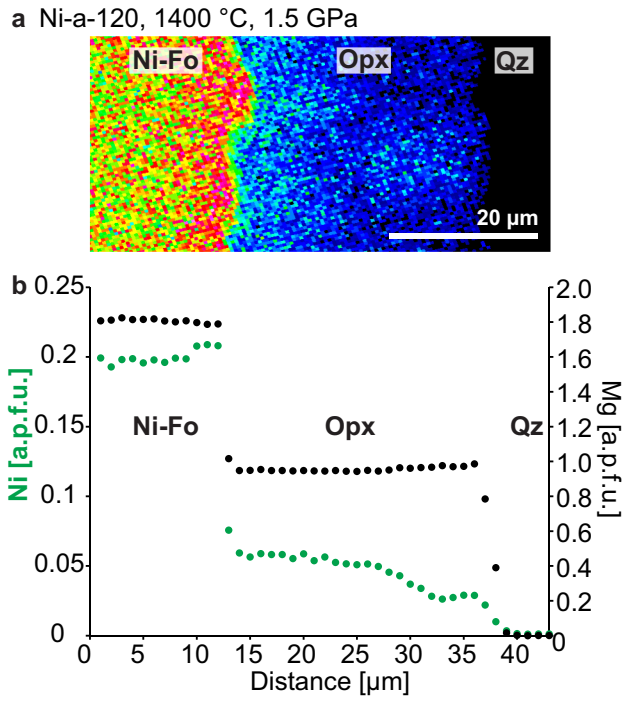

Fig. 5 Ni-distribution map (same general colour coding as in Fig. 3) and line scan of sample Ni-a-120. The line scan was acquired with a step size of 1 µm. Both data demonstrate Ni-enrichment in Ni-Fo ahead of the replacement front. Ni concentration in the Opx rim decreases from the Ni-Fo|Opx interface towards the opposite Opx|Qz interface. Grain boundaries appear to be depleted in Ni relative to their grain interiors. Sizes of symbols exceed errors

around Ni-doped forsterite relative to rims that formed around Co-doped forsterite (6.7 ± 0.4) µm^2/h and natural San Carlos olivines (7.2 ± 0.4) µm^2/h under similar experimental conditions, i.e., 1.4 GPa and 1000 °C. In fact, the rim growth rate of (1.4 ± 0.2) µm^2/h for Opx rim growth around Ni-doped forsterite matches much better the data of Yund (1997) obtained from experiments on San Carlos olivines performed under 0.7 GPa and 950 °C (1.4 ± 0.4) µm^2/h (Fig. 7).

Discussion

Chemical distribution patterns

Manganese and zinc display very similar distribution patterns with a Mn- or Zn-enriched part of the outer Opx rim next to Qz (Fig. 6) resembling the fractionation behavior previously described for Fe (Milke et al. 2011). Thus, analogous to the distribution behavior of Fe, equilibrium partitioning between (Mn, Zn)-Fo and (Mn, Zn)-Opx results in the release of excess Mn or Zn. Any excess Mn or Zn diffuses along Opx grain boundaries towards the opposite Opx|Qz interface where the dopants are not buffered and will be incorporated in the Opx replacing Qz. Similar chemical distribution patterns to those that form in Opx around Mn- and Zn-doped forsterite as well as around natural Fe-bearing olivines (Milke et al. 2011) were previously reported in rim growth experiments where a titanite rim formed around Nb-bearing rutile grains in a wollastonite matrix under hydrous conditions (Lucassen et al. 2012). It is expected that the distribution behavior and the underlying mechanisms during reaction rim growth are a general phenomenon in exchange reactions where the reactants chemically communicate via the grain-boundary network of the product rim.

The rim that developed around Ni-doped forsterite in the Ni–h-48 sample does not show differences in chemical composition between the Opx part that replaced Ni-Fo and the Opx that consumed Qz (Fig. 2c, d), which is probably due to the precipitation of Ni-rich spheres within the Opx rim. Their occurrence either indicates that under hydrous experimental conditions Ni-saturation in Opx was surpassed or that the presence of minor S due to contamination of the Ni-Fo surface stabilizes Ni-rich spheres. A further investigation of the occurrence and the distribution of S-rich spheres was beyond the scope of the present study.

Ni distribution patterns in the Ni-a-120 sample demonstrate clear Ni-enrichment fronts in the relict Ni-Fo grains ahead of the Ni-Fo-replacement front. This enrichment front indicates that the released Ni was favorably incorporated into Ni-Fo as already observed and described by Milke et al. (2011). Because we used a starting material showing a much higher initial Ni-concentration than Milke et al. (2011), we were able to measure the chemical zoning within the Opx rim showing a Ni-richer Opx part next to the Ol|Opx interface relative to the opposite Opx|Qz interface (Fig. 5). Thus, the observed chemical distribution pattern with a Ni-enrichment front in Ni-Fo and a decreasing Ni-concentration from the Ni-Fo-replacement front towards the opposite interface favors the scenario modeled by Milke et al. (2011) assuming a partition coefficient of around 4.1 (Podvin 1988) and a ratio of volume to grain boundary diffusion in Opx of approx. 1 (Fig. 5 in Milke et al. 2011).

Strikingly, Co as dopant element shows a distribution behavior different to those of Mn, Zn, Fe and Ni. Co exhibits a combination of the Mn-Zn-Fe and the Ni-distribution behaviors. It appears that some excess Co, released during Co-Fo replacement by Co-Opx, has been incorporated into Co-Fo to produce an enrichment front in Co-Fo ahead of the replacement front like Ni. Like Mn, Zn, and Fe, the remaining Co diffuses along Opx grain boundaries towards the opposite interface where it is not buffered. Strikingly, differences in water fugacity do not influence the chemical zoning patterns; except for Ni showing the precipitation of Ni-rich spheres under hydrous conditions. Thus, differences in element distribution within the rim phase and the relict d-Fo must be dopant specific. In order to explain these

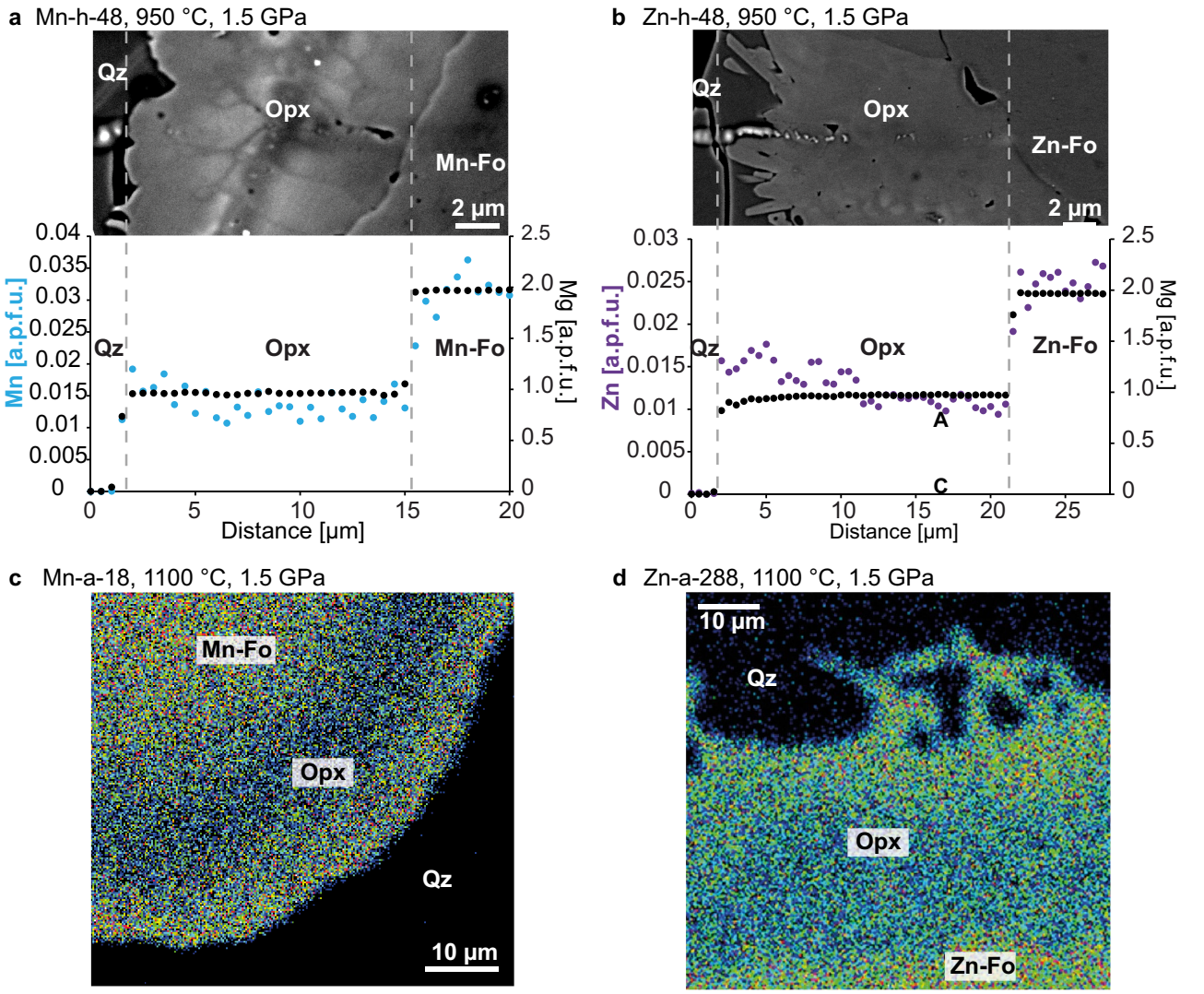

Fig. 6 Results of chemical analyses and element-distribution maps (same general colour coding as in Fig. 3) of the samples in which Mn- and Zn-doped olivines were used. **a** It appears that the outer part of the Opx rim is slightly enriched in Mn relative to the inner part next to Mn-Fo. **c** The same pattern, in this case much clearer, developed in the Opx rim under nominally anhydrous conditions. **b**, **d** Zn-h-48 and Zn-a-288 exhibit Zn-enrichment in the outer Opx part next to Qz. Sizes of symbols exceed errors

different chemical zoning pattern, we need to look closer at the dopant specific partitioning behavior between doped forsterite and Opx.

Element partitioning at the Fo|Opx interface

In an exchange reaction, the preference of an element to be either incorporated in phase A or B is expressed by the partition or distribution coefficient K_D. The large partition coefficient of ~ 4.1 for Ni between olivine and orthopyroxene ($K_{D,Ni}^{Ol/Opx}$) indicates that Ni favorably concentrates in olivine (Gregoire et al. 2000), matching well with our observations that once released at the Ni-Fo-replacement front, Ni will be incorporated into Ni-Fo (Fig. 5). The partition coefficients for Zn and Fe are with 1.5 and 1.2 very close (Dupuy et al. 1987; Seckendorff and Neill 1993) and both dopant elements show a very similar distribution behavior during Opx rim growth (Fig. 6b). In both cases, the excess Fe or Zn diffuses along Opx grain boundaries towards the opposite interface forming an Opx enriched in Zn and Fe relative to the equilibrium Opx replacing Ol or Zn-Fo. Mn has with ~ 1.1 a lower $K_{D,Mn}^{Ol/Opx}$ than Fe and Zn and (Nishizawa and Matsui 1972), thus, the Mn-gradient within the Opx rim is less prominent than for Zn and Fe (Fig. 6). Strikingly, Co has a $K_{D,Co}^{Ol/Opx}$ of around 2.6 (Gregoire et al. 2000) and thus lies in between the values for Ni and Fe or Zn partitioning between Ol and Opx. This intermediate partition coefficient for Co between Ol and Opx could thus explain the mixed distribution behavior we observe in our experiments on Co-doped forsterite.

Due to the higher preference of Co to be incorporated in Ol relative to Opx, some part of the Co released at the Co-Fo-replacement will be incorporated into Co-Fo and the other part diffuses towards the Opx|Qz interface. Further, it appears that Co is mostly located in the Opx rims and the adjacent Opx grain boundaries. This implies that Co preferentially concentrates in the Opx grain boundaries and starts to diffuse into the Opx-grain interiors to equilibrate the gradient in Co concentration between Opx grain interiors and Opx grain rims (Fig. 3).

Milke et al. (2011) stated that the overall chemical distribution of Fe, Ni, and Mg is mostly controlled by kinetic fractionation throughout the Opx rim rather than by equilibrium partitioning at the Ol|Opx interface. Although this is true for Fe, Mg, Zn, the influence of kinetic fractionation on element distribution decreases with an increasing partition coefficient between Ol and Opx. Due to the large $K_{D,Ni}^{Ol/Opx}$ the enrichment of Ni in the relict Ni-Fo causes the Opx replacing Ni-Fo to successively incorporate more Ni and the evolving chemical zoning pattern is thus solely controlled by equilibrium partitioning.

Rim structure

The observed larger Opx grain size in Co-a-257, Ni-a-120, and Zn-a-288 relative to Mn-a-18, are most probably the result of grain coarsening with time (Yund 1997). The experiment on Mn-doped forsterite lasted only 18 h compared to other samples that remained at their respective maximum temperature for 120, 257, and 288 h. It has been experimentally shown that the development of an uneven interface, especially the Opx|Qz interface, correlates well with the water fugacity during the experiment (Milke et al. 2009) with nominally dry experimental conditions leading to smooth interfaces (Fisler et al. 1997; Gardés et al. 2011) whereas H_2O concentrations as low as 20 µg/g already lead to an uneven Opx|Qz interface (Milke et al. 2013). Since the Opx|Qz interfaces in our nominally anhydrous samples are very smooth, relative to the Opx|Qz interfaces of the samples that experienced hydrous conditions (Fig. 2), we assume that the water fugacity was significantly lower in the nominally anhydrous runs than in runs in which hydrous CaF_2 was used as confining medium.

Rim growth rates

In silicate reactions, water plays an eminent role, as it acts as catalyst and transport medium supporting reaction progress. It has been experimentally demonstrated that the presence of water has a strong effect on grain boundary

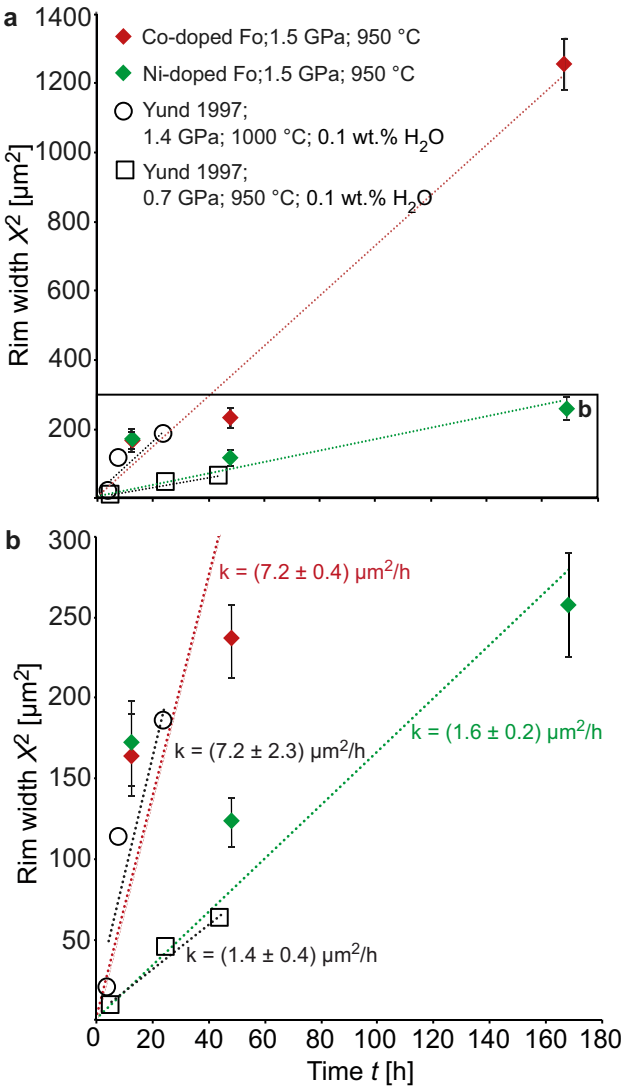

Fig. 7 Time series on Co- and Ni-doped olivine crystals under hydrous conditions. **a** Rim growth rates obtained from experiments on Co-doped forsterite are similar to those from previous experiments on natural olivines conducted at 1.4 GPa and 1000 °C (Yund 1997). **b** Below run durations of 48 h rim growth rates are, within error limits, very similar regardless of the dopant element, but deviate strongly after a run duration of > 12.5 h for Ni-doped Fo

diffusivity governing the rate at which rims grow (Gardés et al. 2011; Götze et al. 2010; Joachim et al. 2012; Milke et al. 2009; Yund 1997; and references therein). The critical water concentration on which the kinetic property, e.g. diffusion coefficient or rate constant, depends can be as low as 20 µg/g H_2O (Milke et al. 2013). When displayed in an Arrhenius plot, the compilation of rim growth data demonstrates two distinct trends (Fig. 8). The sole difference between both trends is the water concentration during the experiment and thus the trends are denoted as 'wet' when performed under hydrous conditions or 'dry' when initial water contents are kept at a minimum (Gardés

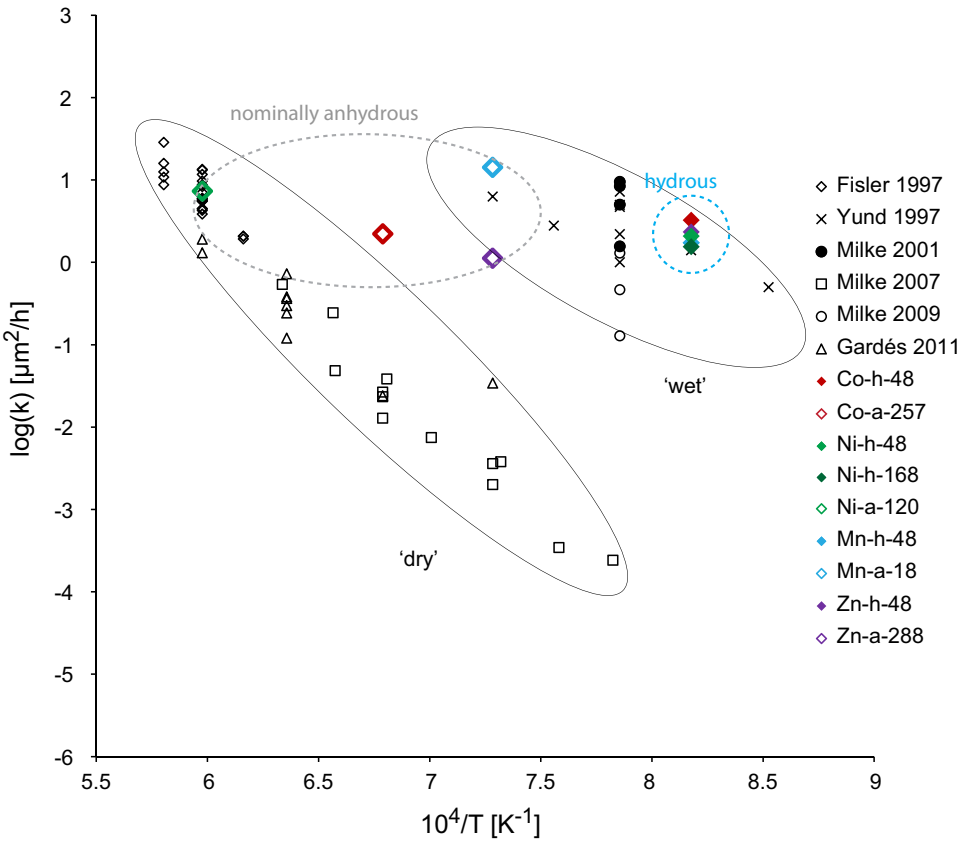

Fig. 8 Compilation of previous Opx rim growth data and our experimental results displayed in a log(k) vs. 10^4/T Arrhenius plot. Rim growth rates of the hydrous samples plot well within the 'wet' regime whereas the data corresponding to the nominally anhydrous samples scatters between the 'dry' and the 'wet' regime. The deviation of the rim growth rates obtained from the nominally anhydrous data is marked by the dashed ellipse. Modified after (Dohmen and Milke 2010)

et al. 2012). Despite some scattering, rim growth data from previous studies does not plot in between these two trends or regimes indicating that the transition from 'dry' to 'wet' regime must occur over a narrow range in water concentration rendering their boundary sharp (Dohmen and Milke 2010).

As expected, the rate constants corresponding to the hydrous samples that stayed under 950 °C for 48 h plot well within the 'wet' regime in the Arrhenius plot (filled diamonds in Fig. 8). Strikingly the data obtained from the nominally anhydrous samples neither uniformly fall within the 'dry' nor the 'wet' regime (hollow diamonds in Fig. 8). The rate constant of Mn-a-18 and Zn-a-288 plot either within or close to the 'wet' regime, the rate constant corresponding to Co-a-257 lies in between both regimes, and the data corresponding to the Ni-a sample clearly plots within the 'dry' regime (Fig. 8).

The observed scattering of the data, corresponding to samples that experienced nominally anhydrous experimental conditions, probably reflects changes in experimental conditions, from hydrous at first to nominally anhydrous due to H_2O loss during the experiment. Truckenbrodt and Johannes (1999) and Patino Douce and Beard (1994) have experimentally shown that above 1000 °C samples lose a significant amount of H_2O of up to 80% after 6 d in the piston-cylinder apparatus. Since every sample that experienced nominally anhydrous conditions remained well above 1000 °C for several days (5–12 d), we expect that most of the H_2O, which was initially present due to adhesion from air humidity, was lost during the runs; except probably for Mn-a-18 which stayed at 1100 °C for only 18 h. The fact that samples lose most H_2O during piston-cylinder runs conducted above 1000 °C agrees with our microstructural observations on the Opx-interface structures showing smoother Opx|Qz interfaces in the samples that were performed using crushable alumina relative to the rim structures in samples in which CaF_2 was used as confining medium (Fig. 2). Another argument for a successive loss of water during the piston-cylinder experiments is that the samples, conducted at the lowest temperature of 1100 °C (Mn-a-18 and Zn-a-288), plot much closer to the wet regime, because outwards diffusion of water from the sample interior towards the confining medium highly depends on temperature with a positive correlation between temperature and diffusion rate. Therefore, water loss was less extensive in samples Mn-a-18 and Zn-a-288 relative to Co-a-257, performed under 1200 °C and hold for 10.7 d, and especially Ni-a-120 that experienced 1400 °C for 5 d. The observed deviation of the rate constants of the nominally anhydrous samples therefore reflects the rates at which the samples dried out due to the loss of water to the confining medium.

Conclusion and implications

The most prominent model reaction for metasomatism in Earth's upper mantle is orthopyroxene rim growth between olivine and quartz. Natural olivine crystals can contain various amounts of minor and trace elements. During the interaction between the olivine-rich mantle and a SiO_2-rich fluid or melt, these elements will distribute between the solid and the fluid phase. Consequently, the mantle olivine as well as the product of this fluid-rock interaction – orthopyroxene – may show particular chemical signatures.

Our experiments on synthetic forsterite doped with the selected metal cations Co, Ni, Mn, Zn reveal that the chemical zoning patterns are dopant specific and depend on their respective partitioning behavior. Water fugacity does not affect the partitioning behavior and the resulting chemical zoning pattern in the rim phase. Because Co and Ni will be favorably incorporated into the doped Fo during Opx rim growth, enrichment in Co and/or Ni in natural olivines may be used to highlight metasomatism in Earth's upper mantle.

Although less relevant for mantle metasomatism in nature, taking place in generally water-present settings and with Ni concentrations in olivine in the ppm range, we observe that in the presence of Ni Opx rim growth rates are slower relative to Opx rim growth around natural San Carlos olivines. However, more experiments are needed to test the influence of the presence of Ni on Opx grain boundary diffusion under hydrous and especially under nominally anhydrous conditions.

Acknowledgements We are very grateful for the detailed comments and the effort of Bastian Joachim-Mrosko, an anonymous reviewer, and journal editor Shah Wali Faryad, which helped improving the manuscript. Further, we would like to thank Giulio Borghini and another anonymous expert who has commented on an earlier version of this manuscript. This study was part of the framework FOR 741 that received funding from the German Science Foundation (DFG). S.I. acknowledges the Alexander von Humboldt Foundation for funding her Feodor-Lynen fellowship. R.M. received funding from the German Science Foundation (DFG) within project MI 1205/2-2.

Funding Open Access funding enabled and organized by Projekt DEAL.

References

Abart R, Kunze K, Milke R, Sperb R, Heinrich W (2004) Silicon and oxygen self diffusion in enstatite polycrystals: The Milke et al. (2001) rim growth experiments revisited. Contrib to Mineral Petrol 147:633–646

Abràmoff MD, Magalhães PJ, Ram SJ (2004) Image Processing with Image J Biophotonics Int 11:36–41

Bloise A, Barrese E, Apollaro C, Miriello D (2009) Flux growth and characterization of Ti- and Ni-doped forsterite single crystals. Cryst Res Technol 44:463–468

Bodinier JL, Vasseur G, Vernieres J, Dupuy C, Fabries J (1989) Mechanisms of Mantle Metasomatism: Geochemical Evidence from the Lherz Peridotite. J Petrol 31:597–628

Borghini G, Rampone E, Zanetti A, Class C, Cipriani A, Hofmann AW, Goldstein SL (2016) Pyroxenite layers in the northern apennines' upper mantle (Italy)-Generation by pyroxenite melting and melt infiltration. J Petrol 57:625–653

Borghini G, Rampone E, Zanetti A, Class C, Cipriani A, Hofmann AW, Goldstein SL (2013) Meter-scale Nd isotopic heterogeneity in pyroxenite-bearing ligurian peridotites encompasses global-scale upper mantle variability. Geology 41:1055–1058

Borghini G, Rampone E, Zanetti A, Class C, Fumagalli P, Godard M (2020) Ligurian pyroxenite-peridotite sequences (Italy) and the role of melt-rock reaction in creating enriched-MORB mantle sources. Chem Geol 532:119252

Chakraborty S (1997) Rates and mechanisms of Fe-Mg interdiffusion in olivine at 980°-1300 °C. J Geophys Res B Solid Earth 102:12317–12331

Cvetković V, Lazarov M, Downes H, Prelević D (2007) Modification of the subcontinental mantle beneath East Serbia: Evidence from orthopyroxene-rich xenoliths. Lithos 94:90–110

Dohmen R, Milke R (2010) Diffusion in polycrystalline materials: Grain boundaries, mathematical models, and experimental data. In: Zhang Y, Cerniak DJ (eds) Diffusion in minerals and melts. Rev Mineral Geochem, 72. Miner Soc Am, Chantilly VA, 921–970

Dupuy C, Dostal J, Bodinier JL (1987) Geochemistry of spinel peridotite inclusions in basalts from Sardinia. Mineral Mag 51:561–568

Fisler DK, Mackwell SJ, Petsch S (1997) Grain boundary diffusion in enstatite. Phys Chem Miner 24:264–273

Gardés E, Wunder B, Marquardt K, Heinrich W (2012) The effect of water on intergranular mass transport: New insights from diffusion-controlled reaction rims in the MgO-SiO_2 system. Contrib to Mineral Petrol 164:1–16

Gardés E, Wunder B, Wirth R, Heinrich W (2011) Growth of multilayered polycrystalline reaction rims in the MgO-SiO_2 system, part I: Experiments. Contrib to Mineral Petrol 161:1–12

Götze LC, Abart R, Rybacki E, Keller LM, Petrishcheva E, Dresen G (2010) Reaction rim growth in the system MgO-Al_2O_3-SiO_2 under uniaxial stress. Mineral Petrol 99:263–277

Gregoire M, Moine BN, O'Reilly SY, Cottin JY, Giret A (2000) Trace element residence and partitioning in mantle xenoliths metasomatized by highly alkaline, silicate- and carbonate-rich melts (Kerguelen Islands, Indian Ocean). J Petrol 41:477–509

Hidas K, Borghini G, Tommasi A, Zanetti A, Rampone E (2021) Interplay between melt infiltration and deformation in the deep lithospheric mantle (External Liguride ophiolite, North Italy). Lithos 380–381:105855

Joachim B, Gardés E, Velickov B, Abart R, Heinrich W (2012) Experimental growth of diopside + merwinite reaction rims: The effect of water on microstructure development. Am Mineral 97:220–230

Joesten R (1991) Grain-boundary diffusion kinetics in silicate and oxide minerals. In: Kubicki JD, Lasaga AC, Ganguly J (eds) Diffusion, atomic ordering, and mass transport. Springer, New York, pp 345–395

Kelemen PB, Hart SR, Bernstein S (1998) Silica enrichment in the continental lithosphere via melt / rock reaction. Earth Planet Sci Lett 164:387–406

Lucassen F, Franz G, Rhede D (2012) Small-scale transport of trace elements Nb and Cr during growth of titanite: An experimental study at 600 °C, 0.4 GPa. Contrib to Mineral Petrol 164:987–997

Milke R, Abart R, Keller L, Rhede D (2011) The behavior of Mg, Fe, and Ni during the replacement of olivine by orthopyroxene: experiments relevant to mantle metasomatism. Mineral Petrol 103:1–8

Milke R, Dohmen R, Becker HW, Wirth R (2007) Growth kinetics of enstatite reaction rims studied on nano-scale, Part I: Methodology, microscopic observations and the role of water. Contrib to Mineral Petrol 154:519–533

Milke R, Kolzer K, Koch-Müller M, Wunder B (2009) Orthopyroxene rim growth between olivine and quartz at low temperatures (750–950°C) and low water concentration. Mineral Petrol 97:223–232

Milke R, Neusser G, Kolzer K, Wunder B (2013) Very little water is necessary to make a dry solid silicate system wet. Geology 41:247–250

Milke R, Wiedenbeck M, Heinrich W (2001) Grain boundary diffusion of Si, Mg, and O in enstatite reaction rims: a SIMS study using isotopically doped reactants. Contrib to Mineral Petrol 142:15–26

Nishizawa O, Matsui Y (1972) An experimental study on partition of magnesium and manganese between olivine and orthopyroxene. Phys Earth Planet Inter 6:377–384

Patino Douce AE, Beard JS (1994) H_2O loss from hydrous melts during fluid-absent piston cylinder experiments. Am Mineral 79:585–588

Petry C, Chakraborty S, Palme H (2004) Experimental determination of Ni diffusion coefficients in olivine and their dependence on temperature, composition, oxygen fugacity, and crystallographic orientation. Geochim Cosmochim Acta 68:4179–4188

Podvin P (1988) Ni-Mg partitioning between synthetic olivines and orthopyroxenes: Application to geothermometry. Am Mineral 73:74–280

Seckendorff V, Neill HSCO (1993) An experimental study of Fe-Mg partitioning between olivine and orthopyroxene at 1173, 1273 and 1423 K and 1.6 GPa. Contrib to Mineral Petrol 113:196–207

Spandler C, O'Neill HSC (2010) Diffusion and partition coefficients of minor and trace elements in San Carlos olivine at 1,300 °C with some geochemical implications. Contrib to Mineral Petrol 159:1–28

Truckenbrodt J, Johannes W (1999) H_2O loss during piston-cylinder experiments. Am Mineral 84:1333–1335

Wulff-Pedersen E, Neumann E-R, Vannucci R, Bottazzi P, Ottolini L (1999) Silicic melts produced by reaction between peridotite and infiltrating basaltic melts: ion probe data on glasses and minerals in veined xenoliths from La Palma, Canary Islands. Contrib to Mineral Petrol 137:59–82

Yund RA (1997) Rates of grain boundary diffusion through enstatite and forsterite reaction rims. Contrib to Mineral Petrol 126:224–236